

RESEARCH

Open Access



# Disulfidoptosis-related subtype and prognostic signature in prostate cancer

Zhen Kang<sup>1,2†</sup>, Zheng-Hua Wan<sup>1,2†</sup>, Rui-Cheng Gao<sup>1,2†</sup>, Dong-Ning Chen<sup>1,2</sup>, Qing-Shui Zheng<sup>1,2</sup>, Xue-Yi Xue<sup>1,2,3</sup>, Ning Xu<sup>1,2,3</sup> and Yong Wei<sup>1,2\*</sup>

## Abstract

**Background** Disulfidoptosis refers to cell death caused by the accumulation and bonding of disulfide in the cytoskeleton protein of SLC7A11-high level cells under glucose deprivation. However, the role of disulfidoptosis-related genes (DRGs) in prostate cancer (PCa) classification and regulation of the tumor microenvironment remains unclear.

**Methods** Firstly, we analyzed the expression and mutation landscape of DRGs in PCa. We observed the expression levels of SLC7A11 in PCa cells through in vitro experiments and assessed the inhibitory effect of the glucose transporter inhibitor BAY-876 on SLC7A11-high cells using CCK-8 assay. Subsequently, we performed unsupervised clustering of the PCa population and analyzed the differentially expressed genes (DEGs) between clusters. Using machine learning techniques to select a minimal gene set and developed disulfidoptosis-related risk signatures for PCa. We analyzed the tumor immune microenvironment and the sensitivity to immunotherapy in different risk groups. Finally, we validated the accuracy of the prognostic signature genes using single-cell sequencing, qPCR, and western blot.

**Results** Although SLC7A11 can increase the migration ability of tumor cells, BAY-876 effectively suppressed the viability of prostate cancer cells, particularly those with high SLC7A11 expression. Based on the DRGs, PCa patients were categorized into two clusters (A and B). The risk label, consisting of a minimal gene set derived from DEGs, included four genes. The expression levels of these genes in PCa were initially validated through in vitro experiments, and the accuracy of the risk label was confirmed in an external dataset. Cluster-B exhibited higher expression levels of DRG, representing lower risk, better prognosis, higher immune cell infiltration, and greater sensitivity to immune checkpoint blockade, whereas Cluster A showed the opposite results. These findings suggest that DRGs may serve as targets for PCa classification and treatment. Additionally, we constructed a nomogram that incorporates DRGs and clinical pathological features, providing clinicians with a quantitative method to assess the prognosis of PCa patients.

**Conclusion** This study analyzed the potential connection between disulfidoptosis and PCa, and established a prognostic model related to disulfidoptosis, which holds promise as a valuable tool for the management and treatment of PCa patients.

## Introduction

Prostate cancer (PCa) is the second most common cancer in men worldwide, with approximately 1.3 million new cases diagnosed each year globally [1]. Advances have been made in the treatment of PCa patients over the past few decades, and options for treating prostate cancer include surgery, radiation therapy, chemotherapy, and hormone therapy [2]. However, the effectiveness of these

<sup>†</sup>Zhen Kang, Zheng-Hua Wan, and Rui-Cheng Gao have contributed equally to this work.

\*Correspondence:

Yong Wei

weiyong2017@fjmu.edu.cn

Full list of author information is available at the end of the article



treatments for prostate cancer is limited. Five percent of PCa cases are found to have metastasized at the time of initial diagnosis, with a five-year survival rate of less than 30% [3]. Therefore, new approaches need to be explored for managing or curing PCa.

Disulfidptosis is a novel form of cell death distinct from ferroptosis, apoptosis, and others. The SLC family member SLC7A11 transporter plays a crucial role in maintaining intracellular glutathione levels and protecting cells from oxidative stress-induced cell death [4]. Recent studies have shown that under glucose starvation conditions, in cells with high levels of SLC7A11, increased NADPH consumption and disulfide stress can induce the formation of disulfide bonds in redox-sensitive proteins and a large accumulation of small-molecule disulfides, leading to a series of redox defects and cell death, hence the term disulfidptosis [5].

Currently, there is no research on the relationship between PCa and disulfidptosis. We discovered an inhibitory effect induced by a glucose transporter inhibitor on tumours with high SLC7A11 expression via in vitro PCa experiments. To explore the connection between disulfidptosis and PCa progression and provide a new therapeutic approach for PCa, we obtained 901 PCa samples from the TCGA, GEO, and MSKCC databases; analysed the differences in the expression of disulfidptosis-related genes in PCa samples; assessed their correlation with the survival of PCa patients; and constructed disulfidptosis-related clusters and risk models, which can be used as tools for analysing treatment, the immune microenvironment and prognosis.

## Materials and methods

### Public data acquisition

The TCGA-PRAD second-generation sequencing data and tumour gene mutation-related data were obtained from the TCGA database (<https://portal.gdc.cancer.gov/>). The "GSE70770" and "GSE46602" datasets were downloaded from GEO (<https://www.ncbi.nlm.nih.gov/geo/>), and the prostate adenocarcinoma (MSKCC, Cancer Cell 2010) dataset was downloaded from the Fudan Data Portal (<https://data.3steps.cn/cdataportal/>). The "sva" package was utilized to merge the GSE70770, MSKCC, and TCGA-PRAD data (co-PCa). The patient ID is represented on the x-axis, whereas the gene names are displayed on the y-axis. The 24 DRGs are sourced from the literature records of Xiaoguang Liu et al. [5].

The clinical data for the TCGA-PRAD cohort, updated in April 2022, were used. "Biochemical recurrence" was considered the disease progression status. The biochemical recurrence of prostate cancer is defined as the occurrence of biochemical recurrence of prostate cancer if the PSA concentration exceeds 0.2 ng/mL two consecutive

times after radical surgery or radical radiotherapy but no recurrent or metastatic lesions are found on imaging [6, 7]. "days\_to\_first\_biochemical\_recurrence" represents the disease progression time. In cases where "days\_to\_first\_biochemical\_recurrence" was not recorded, "days\_to\_last\_followup" was employed as the disease progression time, and "has\_new\_tumor\_events\_information" was used as the disease progression status. In GSE70770, "biochemical relapse" represented the disease progression status, and "time to bcr" denoted the disease progression time. In GSE46602, "bcr" was utilized as the disease progression status, and "bcr\_free\_time" was used as the disease progression time. In the MSKCC cohort, "disease-free status" served as the indicator of disease progression, whereas "disease-free status" indicated the time of tumour occurrence and progression.

### Potential relationship between DRGs and prostate cancer

The "maftools" package in R [8] was used to process TCGA mutation gene data, and Perl was used to analyse gene copy number variations in prostate cancer. The "limma" package [9] was used to analyse differential DRGs between normal prostate tissue and cancer tissue in the TCGA database.

### PCR and WB experiments

RNA was extracted from cells such as RWPE-1, PC-3, and DU145 cells via the TRIzol reagent (Invitrogen, Carlsbad, CA). After the RNA concentration was measured via a nanospectrophotometer, the extracted RNA was converted to cDNA via a reverse transcription kit (TransGen Biotech). Specific primers for the target genes were designed at NCBI (Supplementary Table S1) and synthesized by Shangya Biotechnology Co., Ltd. (Fuzhou, China). qPCR amplification was performed by mixing appropriate amounts of cDNA, gene-specific primers, ddH<sub>2</sub>O, and 2× Taq Pro Universal SYBR qPCR Master Mix. The relative expression level of the target gene was calculated via the use of GAPDH as the reference gene and the 2- $\Delta\Delta$ ct method. For protein analysis, we extracted proteins from different cell types via RIPA buffer after the addition of a protease inhibitor. The protein concentration was measured via a BCA protein concentration assay kit. Equal amounts of protein samples (20  $\mu$ g) were subsequently mixed with SDS sample buffer and heated at 95 °C for 5 min to denature the proteins. The proteins were then separated by SDS-PAGE, with the gel concentration selected on the basis of the molecular weight of the target proteins. Following electrophoresis, the proteins were transferred from the gel to a PVDF membrane prewet with methanol via the wet transfer method. After transfer, the PVDF membrane was blocked

with 5% nonfat dry milk or BSA for 1 h to prevent non-specific antibody binding. The membrane was then incubated overnight at 4 °C with a primary antibody specific to the target protein. The membrane was washed three times with TBST (TBS + Tween 20), with each wash lasting 10 min. The membrane was subsequently incubated with an HRP-conjugated secondary antibody at room temperature for 1 h, followed by three washes with TBST, each lasting 10 min. Protein expression was detected via enhanced chemiluminescence, and signals were captured via an imaging system for band density analysis.

#### Plasmid transfection

The SLC7A11 overexpression plasmid and empty plasmid were transiently transfected into the DU145 and PC-3 cell lines via Lip8000. After transfection for 24 h, RNA and protein were extracted to verify the transfection efficiency.

#### CRISPR-Cas9 dual-vector lentiviral system construction and SLC7A11 knockout

To knock out the SLC7A11 gene in DU145 and PC-3 cells, we used a CRISPR-Cas9 dual-vector lentiviral system. This system delivers Cas9 protein and sgRNA via two separate lentiviruses, with the Cas9 vector carrying a puromycin resistance gene. The specific sgRNA sequences targeting SLC7A11 are provided in Table S1. DU145 and PC-3 cells were seeded in 6-well plates, and when cell confluence reached approximately 30%, Lenti-Cas9 lentivirus was used for infection. After infection, puromycin was added for selection to establish a stable mixed clonal cell line expressing Cas9. Following selection, these cells were infected with Lenti-sgRNA lentivirus, and the cells were subsequently harvested for further analysis. For sgRNA lentiviruses with neomycin resistance, G418 was used to eliminate cells that were not successfully infected.

#### IC<sub>50</sub> of BAY-876 in prostate cancer cell lines

PC-3 and DU-145 cells were seeded in a 96-well plate, with approximately 4000 cells per well. The experimental cluster, DMSO cluster, and blank control cluster were each set up with 5 replicate wells, and 100 µl of complete culture medium was added to each well. After 24 h of cell attachment and growth, the culture medium was aspirated from each well. BAY-876 was dissolved in DMSO and added to the experimental cluster at various concentrations in the culture medium (25 µM, 12 µM, 6 µM, 3 µM, 1.5 µM, and 0.7 µM), while the blank control cluster received culture medium without the drug. The plate was placed in an incubator and cultured for 0, 24, 48, or 72 h. At each time point, the culture medium was aspirated from each well, and 100 µl of culture medium

containing CCK-8 was added. The volume of CCK-8 was 1/10 of the cell culture medium volume. After the plate was incubated for an additional 2 h in the incubator, the cell viability was measured via an enzyme-linked immunosorbent assay (ELISA) reader at a wavelength of 450 nm.

#### Cell function experiments

After transfecting the SLC7A11 plasmid into DU145 and PC-3 cells, we performed wound healing and Transwell migration/invasion assays to assess the impact of SLC7A11 on cell migration and invasion abilities. In the wound healing assay, an artificial scratch was created on the cell monolayer, and cell migration into the wound area was observed and measured over 24 h to evaluate the migration capacity of the cells. For the Transwell assay, transfected cells were placed in the upper chamber of a Transwell insert, with serum-free medium in the upper chamber and medium containing 30% serum in the lower chamber. After 36 h, the number of cells that migrated through the membrane and adhered to the lower side was quantified to assess the migration and invasion abilities of the cells. On the basis of the IC<sub>50</sub> values calculated from the above steps, BAY876 (25 µM, 12 µM, 6 µM, 3 µM, 1.5 µM, and 0.7 µM) was added to prostate cancer cell lines transfected with SLC7A11, and a CCK-8 assay was performed. Cell viability was compared among the SLC7A11 overexpression group, plasmid empty vector group and control group in DU145 and PC3 cells.

#### Assessment of apoptosis via flow cytometry

To evaluate the effect of SLC7A11 knockout on cell apoptosis, we conducted flow cytometry analysis on DU145 and PC-3 cells. The cells were cultured in glucose-containing and glucose-free media for 16 h. After incubation, apoptosis was assessed using an Annexin V-FITC/7-AAD double-staining kit (Beyotime, China) following the manufacturer's instructions. Specifically, cells were harvested and washed with PBS, then resuspended in binding buffer. Subsequently, 5 µL of Annexin V-FITC and 5 µL of 7-AAD were added to 100 µL of the cell suspension and incubated in the dark for 10 min. Flow cytometry was performed using a BD FACSCalibur flow cytometer (BD Biosciences, USA), and data were analyzed with FlowJo software (Version X.0.7, Tree Star, USA) to distinguish early and late apoptotic cells.

#### Immunohistochemistry

Immunohistochemistry (IHC) was performed on a total of 6 tissue specimens, including 3 prostate cancer and 3 normal prostate tissues, all obtained from the First Affiliated Hospital of Fujian Medical University. The tissues

were fixed in 10% formalin, embedded in paraffin, and sectioned at a thickness of 4  $\mu\text{m}$ . After deparaffinization and rehydration, antigen retrieval was performed using citrate buffer (pH 6.0) in a microwave. The sections were then blocked with 3% hydrogen peroxide to inhibit endogenous peroxidase activity, followed by incubation with primary antibodies against the target proteins at 4 °C overnight. After washing, the sections were incubated with a biotinylated secondary antibody, followed by streptavidin-HRP. Color development was achieved using DAB (3,3'-diaminobenzidine), and the sections were counterstained with hematoxylin. Finally, the slides were dehydrated, mounted, and examined under a light microscope for analysis. The immunohistochemistry results were assessed using semi-quantitative analysis and represented by symbols: "+" indicates low expression, "++" indicates moderate expression, "+++" indicates high expression, and "-" indicates no expression. Each sample was evaluated independently by two pathologists to ensure the accuracy of the results.

#### Disulfidptosis-related classification

Using the R package "ConsensusClusterPlus" [10], unsupervised consensus clustering was performed to divide "co-PCa" into different clusters on the basis of DRGs. The main parameter settings were as follows: clusterAlg=km, distance=Euclidean, and seed=123,456. DRG cluster feature analysis was conducted as follows: differential analysis of progression-free survival (PFS) among different DRG subclusters was performed via the "survival" package. The "GSVA" package [11] was utilized to analyse the biological pathways primarily involved in different subclusters. Single-sample gene set enrichment analysis (ssGSEA) was employed to assess the infiltration of immune cells in different subclusters. The "limma" package was used to identify differentially expressed genes (DEGs) between the two DRG subclusters. Random forest and single-factor Cox regression analyses were conducted on the DEGs to select a minimal gene set for subsequent analysis.

#### Disulfidptosis-related prognostic model

Using the "ConsensusClusterPlus" package again, unsupervised consensus clustering was performed to divide "Co-PCa" into different subclusters on the basis of the DEGs. To distinguish the DRG clusters mentioned in "Materials and Methods 3," they are referred to here as gene clusters. The "survival" package was used to compare the patient survival times among different gene clusters, whereas the "heatmap" package was used to compare the clinical characteristics among different subclusters. Patients were randomly divided into a training set and a

testing set (5:5 ratio). LASSO regression was employed to select risk markers, and a prognostic model was built in the training set to calculate the patient risk scores via the following formula:  $\text{riskScore} = \beta_i * \text{LRG}_i$ , where  $\beta_i$  represents the expression level of the risk gene and  $\text{LRG}_i$  denotes the gene expression coefficient calculated via LASSO regression. The median risk score was used as the cut-off to classify patients into high- and low-risk groups. The survival outcomes of the two clusters were compared to validate the accuracy of the model. Furthermore, the model was validated in the testing set and an external validation set, GSE46602. By integrating the prognostic features and clinical characteristics, a nomogram was generated via the "RMS" package. Calibration curves and time-dependent ROC curves were utilized to evaluate the accuracy of the risk scoring model and the nomogram.

#### Immune correlation

The "ggalluvial" package [12] was used to observe the relationships among the three types of clusters: "DRG-cluster," "gene-cluster," and "risk-cluster." The ESTIMATE algorithm from the "estimate" package was employed to estimate the ratios of immune and stromal components in the tumour microenvironment (TME) for each sample. The "CIBERSORT" package was used to calculate immune cell infiltration in different clusters of PCa patients and to compare the tumour mutation burden (TMB) and gene mutation profiles among different risk groups. The optimal cut-off value for the TMB was determined on the basis of the TMB values in the TCGA-PRAD cohort. Patients were then classified into high-TMB and low-TMB clusters, and the "survival" package was used to analyse the survival differences among these clusters.

#### Performance of the risk signature in PCa

Single-cell sequencing data were obtained from GSE141445 [13]. TISCH (<http://tisch.comp-genomics.org/>) and IMMUcan (<https://immucanscdb.vital-it.ch/>) tools were used to analyse the expression levels of risk-associated genes in different prostate cancer cell populations. The detailed methods were described previously (Materials and Methods 2). qPCR and WB were conducted to assess the expression levels of four Lasso-related genes in various prostate cancer cell lines (PC-3/C4-2/DU145/22RV1/RWPE-1). The Human Protein Atlas (HPA) was used to explore the immunohistochemistry results of risk-associated genes in prostate epithelial tissue and tumour tissue (<https://www.proteinatlas.org/>). The results were statistically analysed on the basis of the proportions in the categories of low, medium, high, and not detected.

## The tools

In this study, the analyses were performed via R-4.1.2 and Perl-5.32.1.1. A significance level of  $P < 0.05$  was considered statistically significant (\* $P$  value  $< 0.05$ ; \*\* $P < 0.01$ ; \*\*\* $P < 0.001$ ). The research workflow diagram and code are provided in the Supplementary Materials and Tables.

## Results

### Connection between PCa and disulfidptosis

In an article by Xiaoguang Liu et al., 24 DRGs were reported (Supplementary Table S2). In the TCGA-PRAD cohort, these DRGs presented no significant mutations (Fig. 1a) or stable expression. Figure 1b shows the localization of the 22 DRGs on the human chromosome. In the TCGA-PRAD cohort, seven genes, such as RPN1, presented copy number losses, and 17 genes, including PDLIM1, presented copy number gains (Fig. 1c). In the TCGA-PRAD tumour samples, four DRGs, NDUFA11, OXSM, RPN1, and SLC7A11, were upregulated, whereas 12 DRGs, including FLNA, were downregulated (Fig. 1d). To further understand the functions of these differentially expressed genes in PCa, we performed Kyoto Encyclopedia of Genes and Genomes (KEGG) enrichment analysis and revealed that, in addition to regulating the "Regulation of the actin cytoskeleton", which plays a key role in disulfidptosis, DRGs also play roles in biological pathways such as "Proteoglycans in cancer", "Ferroptosis" and "Tight junctions" (Supplementary Materials 1). SLC7A11, one of the DRGs, is a key node in disulfidptosis. We discovered that SLC7A11 might promote the progression of PCa (Fig. 1e). To further confirm the role of SLC7A11 in PCa, qPCR detection revealed that SLC7A11 expression levels in PC-3 and DU-145 cells were significantly higher than those in normal prostate epithelial cells (Fig. 1f) (Supplementary Table S1), and WB also revealed higher protein levels of SLC7A11 in PC-3 cells (Fig. 1g). Chen et al. performed single-cell sequencing on 13 cases of PCa and reported the results in GSE141445. We performed single-cell sequencing analysis on the GSE14144 dataset through ImmuscVue

(<https://immucanscdb.vital-it.ch>) and discovered that SLC7A11 is predominantly expressed in malignant cells, suggesting a potential procarcinogenic role of SLC7A11 in the progression of PCa (Fig. 1h, i). The SLC7A11 overexpression plasmid was used to transfect PC-3 and DU145 cells, and the transfection results were verified by WB and PCR (Fig. 1j, k). After confirming the overexpression efficiency, cell scratch and Transwell experiments were performed. In the DU145 (Fig. 1l, m) and PC3 (Fig. 1n, o) SLC7A11-OE groups, the cell migration and invasion ability increased significantly (Supplementary Materials 1). We added the GLUT-1 inhibitor BAY-876 to PC-3 and DU145 cells at concentrations ranging from 25 to 0.7  $\mu\text{mol}$  (25, 12, 6, 3, 1.5, and 0.7). The OD values of the cells at 0, 24, 48, and 72 h after the addition of the drug were measured via a CCK8 assay, which revealed that as the concentration of BAY-876 increased, the cell activity gradually weakened. The IC<sub>50</sub> of PC-3 at 24 h was 0.70, and the IC<sub>50</sub> of DU145 was 2.19 (Fig. 1p, q), which may be related to higher levels of SLC7A11 in PC-3. After SLC7A11 was overexpressed in DU145 and PC-3 cells, different concentrations of BAY-876 were added again to the 96-well plate, and the OD value at 24 h was measured. Compared with those in the control group and the SLC7A11-EV group, the cell viability rate in the SLC7A11-OE group was significantly lower ( $P < 0.05$ ) at concentrations of 1.5  $\mu\text{mol}$ , 3  $\mu\text{mol}$ , 6  $\mu\text{mol}$ , and 12  $\mu\text{mol}$  (Fig. 1r, S2) (Supplementary Table S2). In DU145 and PC3 cells, we used CRISPR-Cas9 technology with two sgRNA to knock out the SLC7A11 gene, and the knockout efficiency was validated by PCR and WB. The PCR results showed that in both DU145 and PC3 cells, the sgRNAs targeting SLC7A11 significantly reduced the mRNA expression levels of the gene (Figure S1 A, C), indicating the successful knockout of SLC7A11 transcripts. Furthermore, the WB results confirmed this finding, with SLC7A11 protein expression significantly reduced in the knockout group, while remaining at a high level in the control group (Figure S1 B, D). These results collectively demonstrate that we

(See figure on next page.)

**Fig. 1** Connection between disulfidptosis-related genes and prostate cancer: **a** Mutation status of DRGs in the TCGA-PRAD cohort. **b** Chromosomal positions of DRGs. **c** Copy number variations of DRGs, with green balls indicating that "loss" is more frequent than "gain" in DRGs, and vice versa. **d** Differential DRGs between normal tissue and tumour tissue in the TCGA-PRAD cohort. **e** Impact of SLC7A11 on PFS. **f, g** qPCR and WB results of SLC7A11 in PC-3, DU-145, and RWPE-1 cells. **h** Results of single-cell sequencing of prostate cancer cells in the GSE141445 dataset and UMAP dimensionality reduction analysis of the distributions of various immune cells and malignant cells. **i** SLC7A11 expression in different prostate cancer cell subsets. **j, k** qPCR and WB were used to verify the plasmid transfection efficiency of SLC7A11 in DU145 and PC3 cells. **l, n** A scratch assay confirmed that SLC7A11 promoted the migration of DU145 and PC3 cells. **m, o** Transwell assays confirmed the role of SLC7A11 in promoting the invasion of DU145 and PC3 cells (triplicates). **p, q** IC<sub>50</sub> values of BAY-876 in PC-3 and DU145 cells. **r** Inhibitory ability of BAY-876 on PC-3 cells in the SLC7A11-OE, SLC7A11-EV, and control groups. **s** Inhibitory ability of BAY-876 on DU145 cells in the SLC7A11-OE, SLC7A11-EV, and control groups

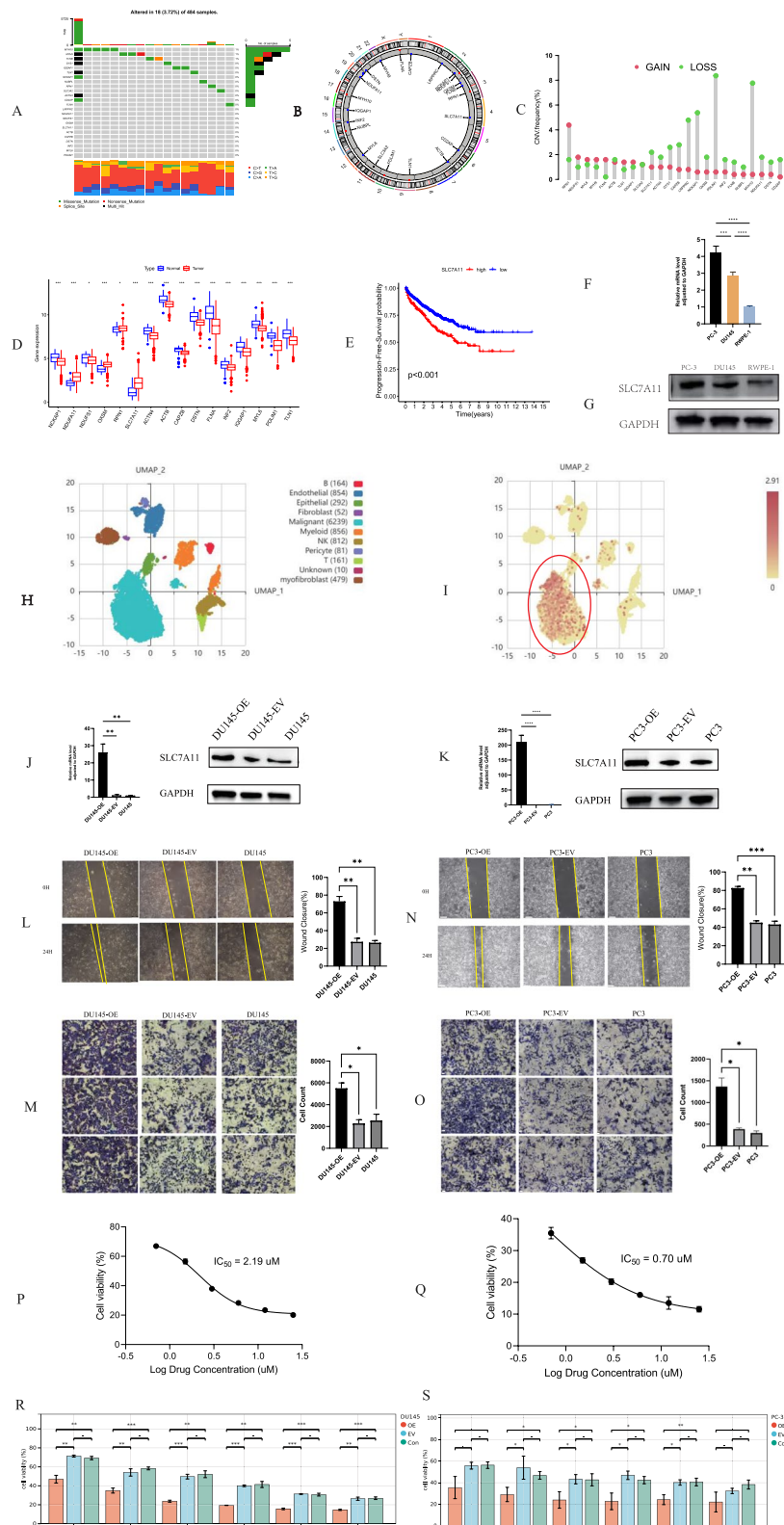


**Fig. 1** (See legend on previous page.)

effectively knocked out SLC7A11 in both DU145 and PC3 cells. To investigate the effect of SLC7A11 knock-out on cell migration, we performed Wound Healing Assay and Transwell migration experiments. In the Wound Healing Assay, compared to the control group, the SLC7A11 knockout group of DU145 and PC3 cells showed significantly inhibited migration capacity, with notably slower wound closure. The quantitative analysis of wound closure further supported this observation (Figure S1 E, F). The Transwell migration experiment results also confirmed that SLC7A11 knockout inhibited the migration capacity of DU145 and PC3 cells. The number of cells migrating through the Transwell chamber significantly decreased in the knockout group, and quantitative analysis indicated that the reduction in migration capacity due to SLC7A11 knockout was statistically significant in both DU145 and PC3 cells (Figure S1 G, H). To further explore the role of SLC7A11 in apoptosis, we performed flow cytometry to assess the apoptosis rates in DU145 and PC3 cells under glucose-free conditions. The results showed that the non-knockout DU145 cells exhibited only a small amount of late apoptosis under glucose deprivation, whereas SLC7A11 overexpression significantly increased late apoptosis. In contrast, SLC7A11 knockout markedly reversed late apoptosis in DU145 cells, with apoptosis rates similar to the control group (Figure S1 I). For PC3 cells, despite the high late apoptosis rate under glucose-free conditions, SLC7A11 overexpression further enhanced late apoptosis. Similar to DU145 cells, SLC7A11 knockout effectively reversed the high apoptosis rate in PC3 cells (Figure S1 J). These results suggest that SLC7A11 plays a key role in regulating cell migration, invasion, and apoptosis, especially under glucose-free conditions. High expression of SLC7A11 leads to increased susceptibility to late apoptosis, while knockout of SLC7A11 significantly reverses this effect, reducing late apoptosis. This indicates that SLC7A11 may play a critical role in the metabolic stress response of tumor cells.

### Disulfidptosis cluster in PCa

To further investigate the relationships between DRGs and PCa, the GSE70770, MSKCC, and TCGA-PRAD

datasets were batch-corrected and merged, resulting in a dataset named Co-Pca. Consensus clustering analysis on the basis of the expression levels of DRGs was performed on the expression profiles of PCa patients. When  $k=2$ , the highest within-cluster correlation was observed, and the 901 PCa patients were divided into two subclusters: DRG Cluster A and DRG Cluster B (Fig. 2a). Principal component analysis (PCA) also confirmed significant differences in the distributions of the two DRG clusters (Fig. 2b). DRG-Cluster B patients had better clinical PFS than did DRG-Cluster A patients ( $P<0.01$ ) (Fig. 2c). GSEA revealed enrichment of pathways such as the WNT, MAPK, and cytoskeleton regulation pathways in DRG Cluster B (Fig. 2d). Additionally, the expression levels of DRGs, including FLNA, FLNB, INF2, IQGAP1, MYH10, MYL6, MYH9, PDLIM1, and TLN1, were greater in DRG Cluster B (Fig. 2e). Compared with DRG-Cluster A, DRG-Cluster B exhibited greater infiltration of CD4+ T cells, B cells, and DCs (Fig. 2f). On the basis of these findings, it was hypothesized that DRG Cluster B represents a subcluster of PCa characterized by increased levels of disulfidptosis, which may not only inhibit tumour progression but also induce immune responses. To further elucidate the biological differences between the two disulfidism clusters, differential gene analysis was performed, resulting in the identification of 877 differentially expressed genes (DEGs) between the two clusters. Among these genes, 20 genes were upregulated in DRG Cluster A, whereas 857 genes were upregulated in DRG Cluster B. After screening with random forest trees (mean decrease Gini  $>5$ ), 87 DEGs were retained (Fig. 2g, h). Further analysis, including single-factor Cox regression analysis and survival data integration, led to the identification of 64 genes that met the criteria for statistical significance ( $P<0.05$ ) (Fig. 2i) (Supplementary Table S3). These DEGs were involved mainly in cellular pathways such as "Focal adhesion," "Proteoglycans in cancer," and "Regulation of the actin cytoskeleton" (Fig. 2j).

### Prognostic model of disulfidptosis in PCa

On the basis of the aforementioned 64 prognosis-related DEGs, a second unsupervised clustering analysis was performed on Co-Pca, revealing that  $k=3$  was the optimal number of clusters (Supplementary Table S3). When  $k=3$ , the intercluster differences were minimized,

(See figure on next page.)

**Fig. 2** Consensus clustering and machine learning based on DRGs in Co-PCa: **a** Co-PCa patients were divided into two clusters via a consensus clustering algorithm. **b** Principal component analysis (PCA) showing the distribution of the two clusters. **c** Differences in PFS between the two clusters. **d** GSEA of biological pathways between the two clusters. **e** Differences in clinical information and DRG expression according to the heatmap. **f** Immune infiltration differences between the two clusters. **g, h** Random forest trees select the minimum set of genes. **i** Cox univariate analysis was used to screen 64 prognosis-related DEGs. **j** KEGG analysis of the biological pathways associated with the DEGs

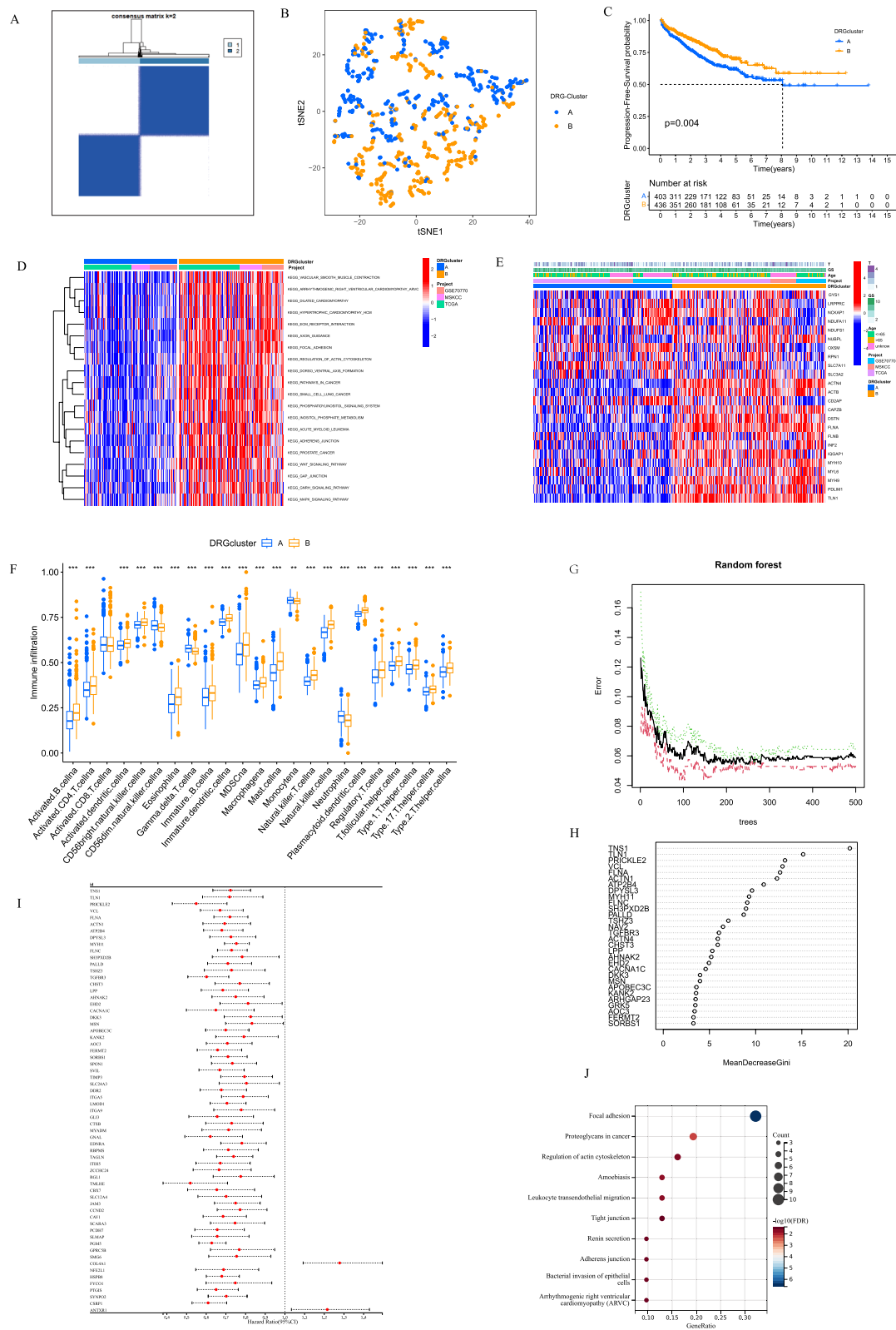


**Fig. 2** (See legend on previous page.)

whereas the intercluster differences were maximized (Fig. 3a). These findings indicate that the 901 PCa patients can be divided into three clusters (I, II, and III) on the basis of the 64 prognosis-related DEGs. K–M survival analysis demonstrated that patients in Cluster I had more rapid tumour progression ( $P < 0.001$ ), whereas patients in clusters II and III had the most favourable prognosis (Fig. 3B). The heatmap (Fig. 3c) displays the associations between DEGs in the two DRG clusters, gene clusters and clinicopathological factors. The gene clusters highly overlapped with Cluster I in DRG Cluster A, whereas cluster III was mostly included in DRG Cluster B. Cluster II was evenly distributed in DRG Clusters A and B, and the disulfidptosis genes were expressed at higher levels in clusters II and III (Fig. 3d). These findings suggest that DRG Cluster B can be further subdivided into two subtypes, but there were no significant differences in clinical characteristics among the clusters. The patients in Co-Pca with complete information (survival time, survival status, and gene expression profile) were subsequently randomly divided into a training set ( $n = 421$ ) and an internal testing set ( $n = 420$ ) at a 5:5 ratio (Supplementary Table S3). LASSO regression and multivariate Cox regression were used in the training set to conduct gene selection and model building (Fig. 3e, f), resulting in the identification of four Lasso-related genes (CTSB, PGM5, COL4A1, and ANTXR1) as risk signatures. The risk score formula was as follows:  $\text{riskScore} = \text{ANTXR} * 0.36287 + \text{COL4A1} * 0.47852 - \text{PGM5} * 0.4575 - \text{CTSB} * 0.5346$ . The median risk score in the training set ( $-1.99$ ) was used as the cut-off to divide patients into high-risk and low-risk groups. K–M analysis demonstrated that the high-risk group had a worse survival prognosis in both the training set and internal testing set ( $P < 0.001$ ) (Fig. 3g, h). Time-dependent receiver operating characteristic (ROC) curves were used to evaluate the sensitivity and specificity of the Lasso model. The 1-year, 3-year, and 5-year AUCs in the training set were 0.731, 0.730, and 0.682, respectively (Fig. 3j), whereas the AUCs in the internal testing set were 0.761, 0.706, and 0.690, respectively (Fig. 3k). To further validate the accuracy of the risk model, the external testing set GSE46602 was used, and patients were stratified into different risk groups on the

basis of the risk score formula. Compared with the low-risk group, the high-risk group exhibited significantly lower PFS (Fig. 3i), with AUCs of 0.82, 0.70, and 0.79 for 1-year, 3-year, and 5-year survival, respectively (Fig. 3l). Combining the previous results, both DRG Cluster A and gene Cluster I had higher risk scores (Fig. 3m, n), and gene cluster II was more unique, as it originated from different DRG clusters and was evenly divided into high-risk and low-risk groups. This made the risk stratification of Cluster I and Cluster III more distinct, with Cluster I predominantly originating from DRG-Cluster A, mostly belonging to the high-risk group, and with Cluster III predominantly originating from DRG-Cluster B, mostly belonging to the low-risk group (Fig. 3O). These results help eliminate confounding factors within subclusters and enhance the prognostic ability of the model.

#### Nomograms and immune correlation of disulfidptosis

By combining the clinical data and Lasso model of Co-Pca, nomograms for predicting PCa progression were constructed by incorporating the tumour T stage, Gleason score (GS), and risk signature (Fig. 4a). The predictive performance of the nomograms was evaluated via ROC curves, with AUCs of 0.758, 0.772, and 0.769 for 1-year, 3-year, and 5-year survival, respectively (Fig. 4b), and a C-index of 0.72. The calibration curve revealed a match between the predicted PCa progression rates and the actual PCa progression rates via the nomograms (Fig. 4c). To further explore the associations between DRGs and the risk signature, the mutation frequency of genes in different risk groups was analysed in the TCGA-PRAD cohort. Genes related to cytoskeletal proteins, such as MYH10, FLNB, and MYH9, harboured missense mutations in the high-risk group (Fig. 4d). These gene mutations may hinder the normal process of disulfidptosis and increase the risk score. Additionally, as the risk score increased, the tumour stemness score also increased ( $R = 0.33$ ), indicating that as the disulfidptosis reaction progressed, the tumour stemness score decreased, and tumour differentiation improved (Fig. 4e). The evaluation of immune cell proportions via Estimate and CIBERSORT revealed higher stromal cell infiltration scores in the high-risk group (Fig. 4f). The stromal components

(See figure on next page.)

**Fig. 3** Gene cluster and prognostic risk label in Co-PCa: **a** Co-PCa patients were divided into three gene clusters on the basis of 64 DEGs via a consensus clustering algorithm. **b** Differences in PFS among the three gene clusters. **c** Heatmap of clinicopathological features and expression of DEGs. **d** DRG expression levels in the 3 gene clusters. **e, f** Selection of the LASSO model; the simulation parameters were set to 1000, tenfold cross-validation was selected, and 4 risk genes were screened. **g–i** Differences in PFS between the low-risk group and the high-risk group in the training group, testing group, and external testing group. **j–l** ROC curve for predicting the 1-, 3-, and 5-year PFS of patients in the training group, testing group, and external testing group. **m** Risk score distribution in two DRG clusters. **n** Risk score distribution in three gene clusters. **o** Connections among the DRG cluster, gene cluster, and risk group

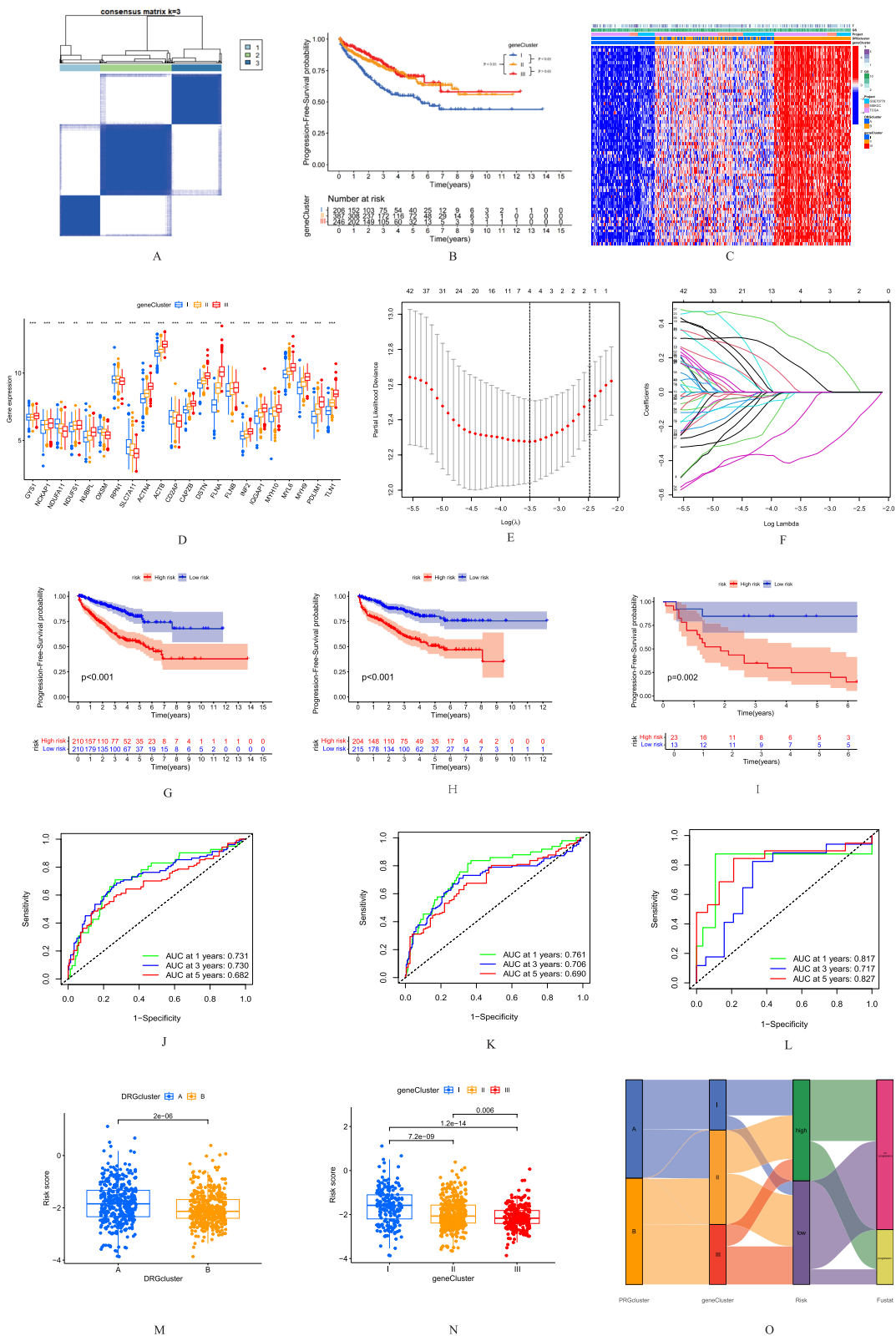


**Fig. 3** (See legend on previous page.)

of the tumour microenvironment (TME) may be more indicative of the prognosis of PCa patients. In contrast, the low-risk group presented increased infiltration of plasma cells, activated NK cells, M0 macrophages, and resting mast cells (Fig. 4g). Among immune cells, PD-L1 expression was significantly greater in the low-risk group (Fig. 4h) and exhibited the most significant negative correlation with plasma cells, activated NK cells, and M0 macrophages (Fig. 4i). The expression levels of the four genes involved in the risk score calculation were significantly different among the different risk groups (Fig. 4j). DC cells, resting mast cells, and CD4 T cells were significantly positively correlated with these model genes, suggesting a potential association between the risk signature and immune cell activity (Fig. 4k). TMB is an indicator of the frequency of gene mutations in tumours. When the frequency of gene mutations in tumour cells is high, the tumour surface carries more tumour antigens, making it more susceptible to attacks from the immune system of the body. In this analysis, the low-risk group had a significantly lower TMB than the high-risk group did (Fig. 4l), and a lower TMB corresponded to a more favourable survival prognosis (Fig. 4m). When considering both the risk score and TMB, the "high-risk group/high-TMB cluster" had the worst prognosis, whereas the "low-risk group/low-TMB cluster" had the most favourable prognosis (Fig. 4n).

#### Expression levels of risk signatures in PCa

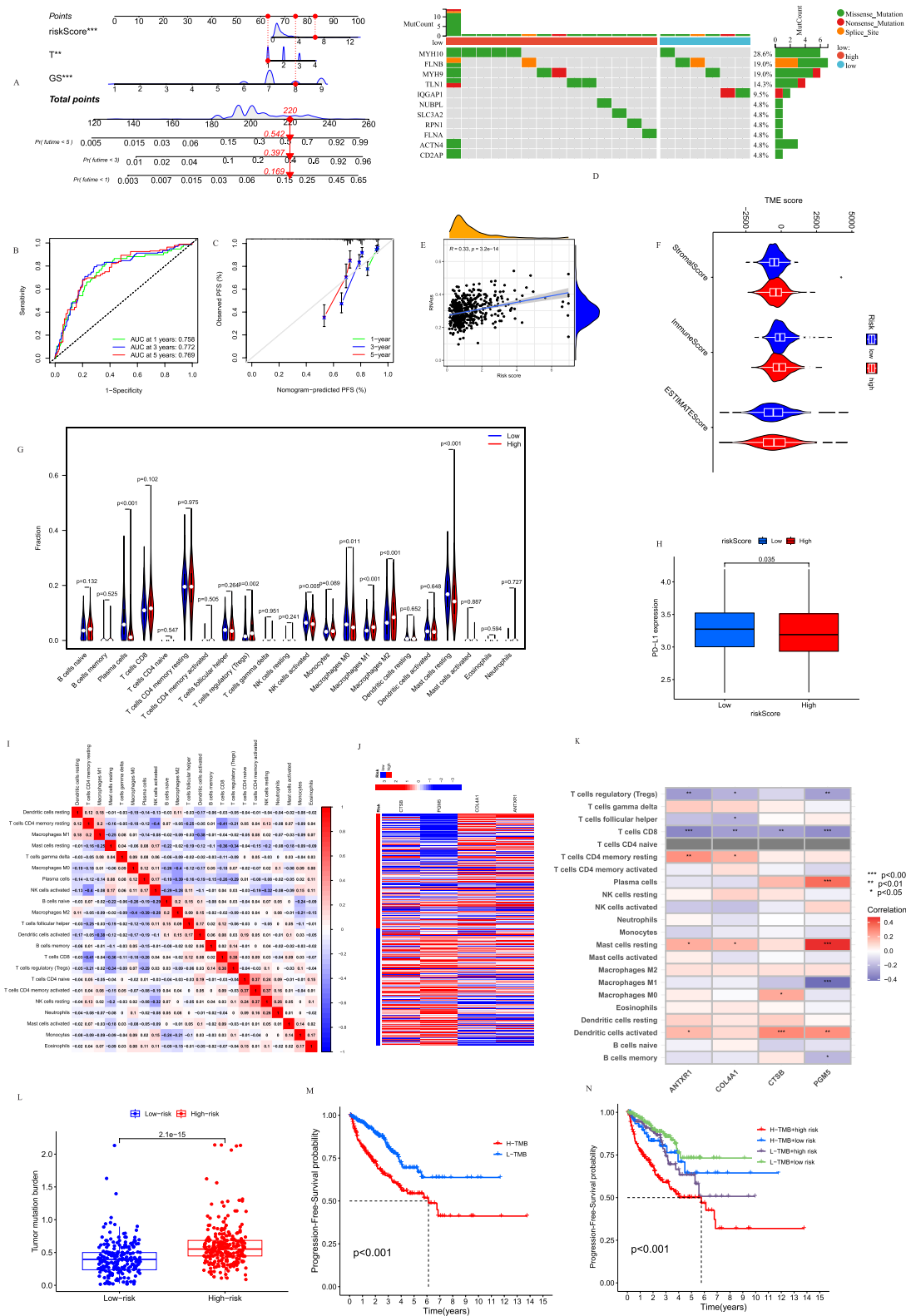
Together, fibroblasts, smooth muscle cells, and infiltrating immune cells form the stroma of the prostate. In the single-cell sequencing dataset GSE141445, PCa was divided into eight cell subtypes, and all four risk signature genes were significantly expressed in fibroblastic epithelial cells (Fig. 5a–f), suggesting their potential impact on tumour development through the regulation of the extracellular matrix (ECM). CTSB and COL4A1 are expressed predominantly in tumour endothelial cells, and active endothelial cells can alter the ECM while reducing immune activity. Previous studies have shown a close relationship between the ECM and the development of PCa, including castration-resistant PCa. As shown in

Fig. 5g, the four risk signature genes and 24 DRGs exhibited varying degrees of correlation (Supplementary Materials 1), with PGM5 and SLC7A11 showing the most significant negative correlation ( $R = -0.31$ ).

The qPCR results (Supplementary Table S1) revealed that ANTXR1, PGM5, and CTSB were upregulated in advanced PCa cell lines compared with the RWPE-1 cell line, whereas their expression levels were lower in early-stage PCa cells, such as 22RV1 and C4-2. COL4A1 was expressed at the highest level in normal epithelial cell lines (Fig. 5h–k). WB results (Fig. 5l) demonstrated the expression of risk signature-related genes in all prostate cancer cell lines. PGM5 was expressed at higher levels in early-stage PCa cells, such as 22RV1 and C4-2 cells, than in normal prostate epithelial cells but at lower levels in DU145 cells. CTSB did not significantly differ in expression between PC-3 cells and normal cells but was expressed at higher levels in other tumour cells. This difference might be due to posttranslational modifications and warrants further investigation. ANTXR1 presented the highest expression in C4-2 cells, whereas COL4A1 presented no significant difference in protein expression among the cell lines. Therefore, further analysis was performed via immunohistochemistry (Fig. 5m–p). According to the results from the HPA (Supplementary Materials 1), COL4A1 showed no positive staining in normal epithelial tissues, and 25% of the tumour tissues presented "low" expression. CTSB showed "high" expression in 67% of normal prostate epithelial cells and "medium" expression in 33%, whereas in cancer tissues, 43% of samples presented "not detected" staining, and CTSB expression was observed in different grades of prostate cancer tissues. PGM5 exhibited "medium" expression in 16% of cancer tissues, and there was no "medium" expression in normal tissues; instead, it was predominantly "low" expression, which was negatively correlated with tumour grade. IHC analysis using clinical specimens revealed significant differences in the expression of ANTXR, COL4A1, CTSB, and PGM5 between normal prostate tissue and prostate cancer tissue (Figure S2). Specifically, ANTXR expression was undetectable in normal prostate tissue (-), while low-level expression

(See figure on next page.)

**Fig. 4** Prognosis and immune microenvironment analysis among the clusters: **a** Nomogram for predicting 1-, 3-, and 5-year PFS in the Co-PCa population on the basis of the risk signature and clinical features. **b** ROC curves of the prognostic nomogram for 1-, 3-, and 5-year survival. **c** Calibration chart of the nomogram. **d** Landscape of DRG mutations in the high- and low-risk groups. **e** Pearson correlation between the risk score and RNAs. **f** The TME score in the high- and low-risk groups. **g** Expression levels of 21 types of immune cells in low-risk and high-risk tumour samples, with the Wilcoxon rank-sum test used for significance. **h** PD-L1 expression levels in the high- and low-risk groups. **i** Heatmap of the correlations among 21 types of immune cells. **j** Heatmap of the differences in the expression of risk signature genes between the high-risk group and the low-risk group. **k** Heatmap of the correlations between 21 types of immune cells and the risk signature. **l** Boxplot of TMB differences between the high-risk group and the low-risk group. **m** PFS of high-TMB and low-TMB patients in the TCGA-PRAD cohort. **n** Comparison of PFS between TCGA-PRAD patients in different risk groups and different TMB levels



**Fig. 4** (See legend on previous page.)

was observed in prostate cancer tissue (+). Similarly, COL4A1 was negative in normal tissues (-) but exhibited moderate expression in prostate cancer tissues (++) . CTSB showed low expression in normal tissues (+) but was absent in prostate cancer tissues (-). PGM5 also demonstrated low expression in normal tissues (+), whereas it was undetectable in prostate cancer tissues (-) (Supplementary Materials 1). These findings suggest that the differential expression patterns of these proteins may play distinct roles in the progression of prostate cancer.

## Discussion

PCa is a unique type of male malignancy characterized by two stages, hormone-sensitive prostate cancer (HSPC) and castration-resistant prostate cancer (CRPC). The progression of PCa is largely driven by the binding of androgens to androgen receptor, which promotes tumor development. Even with aggressive anti-androgen therapy, the median survival period in the CRPC stage is only 2 to 3 years [14]. Furthermore, emerging treatment approaches such as PARP inhibitors and immune checkpoint blockade (ICB) have not shown ideal results in advanced PCa treatment [15, 16]. However, programmed cell death (PCD) offers a new direction for PCa therapy. For instance, during the process of immunogenic cell death (ICD), the release of danger signals from tumor cells can recruit CD8+T cells, potentially enhancing the efficacy of ICB as a cytotoxic lymphocyte-mediated mechanism [17]. Necroptosis of tumor-associated fibroblasts (CAFs) induces a robust immune response through NF- $\kappa$ B signaling [18]. Iron-induced cell death contributes to the anti-tumor effect of CD8+T cells [2], limiting the function of immunosuppressive cells such as tumor-associated macrophages (TAMs) and regulatory T cells (Tregs) within the immunologically "cold" tumor microenvironment. This transformation from an immunosuppressive TME to an inflamed TME enriched with anti-tumor immune cells can also impact the effectiveness of anti-PD-1/PD-L1 immunotherapy. In summary, various forms of PCD can shape the TME and modulate tumor cell growth. These PCD processes in PCa, including iron-induced cell death (Supplementary Materials 1), are unrelated to DRG classification. Therefore, this novel approach to PCD deserves our attention.

PCa itself is a highly SLC7A11-dependent tumor, and theoretically, creating a glucose-deprived environment can induce ferroptosis due to cysteine accumulation. In this study, we found that SLC7A11 can increase tumor cell invasion and migration, but at the same time, we observed a high inhibitory rate of BAY-876 in SLC7A11-overexpressing PC-3 and DU145, indicating that the downstream pathways of disulfidptosis in PCa will be a focus of future research. More importantly, our SLC7A11-KO experiments also revealed a key link between SLC7A11 and disulfidptosis. In glucose-deprived conditions, SLC7A11-KO cells demonstrated a reduced capacity for late apoptosis and disulfidptosis, further confirming the role of SLC7A11 in regulating this form of programmed cell death. These results suggest that SLC7A11 not only promotes cell survival and invasion but also modulates the redox balance in a manner that predisposes cells to disulfidptosis under metabolic stress. Given the unique reliance of prostate cancer cells on SLC7A11 for cystine uptake and redox homeostasis, disulfidptosis presents a promising avenue for targeted therapies, especially in CRPC. The main focus of this article is the multiple classification and prognostic analysis of PCa based on disulfidptosis. Based on the DRG classification, patients were divided into two clusters. DRG-cluster-B showed significant expression of DRGs such as FLNA, FLNB, INF2, which are mainly involved in the regulation of the cellular cytoskeleton [19], and also represent one of the major pathways of disulfidptosis. Therefore, we believe that cluster B represents a population with high levels of disulfidptosis. This population exhibits abundant immune cell infiltration and better patient prognosis, suggesting that disulfidptosis may also influence prognosis by altering the TME.

There are 64 prognosis-related DEGs between DRG-cluster-B and DRG-cluster-A. Based on these DEGs, patients can be further divided into three clusters. Gene-cluster-I is included in DRG-cluster-A and is associated with poor survival prognosis, while gene-cluster-III is included in DRG-cluster-B and is associated with better survival prognosis. Establishing a risk model helps us better understand these clusters. Gene-cluster-II contains both high- and low-risk groups, leading to inconsistent prognosis within this cluster, making accurate

(See figure on next page.)

**Fig. 5** Expression levels of risk labels in prostate cancer cells and tissues. **a-f** Annotation of all cell types and the percentage of each type in GSE141445 and the expression of PGM5, COL4A1, ANTXR1, and CTSB in each cell type. **g** Connection between risk signature genes and DRGs, with purple circles representing risk factors, green circles representing favourable factors, pink lines indicating positive correlations between two factors, and blue lines indicating negative correlations. **h-k** RNA expression levels of the 4 risk signature genes in multiple prostate cancer cell lines. **l** Protein expression levels of the 4 risk signature genes in multiple prostate cancer cell lines, with GAPDH as the reference protein and the thickness of the band representing the protein level. **m-p** Immunohistochemistry results of risk signature genes in the HPA

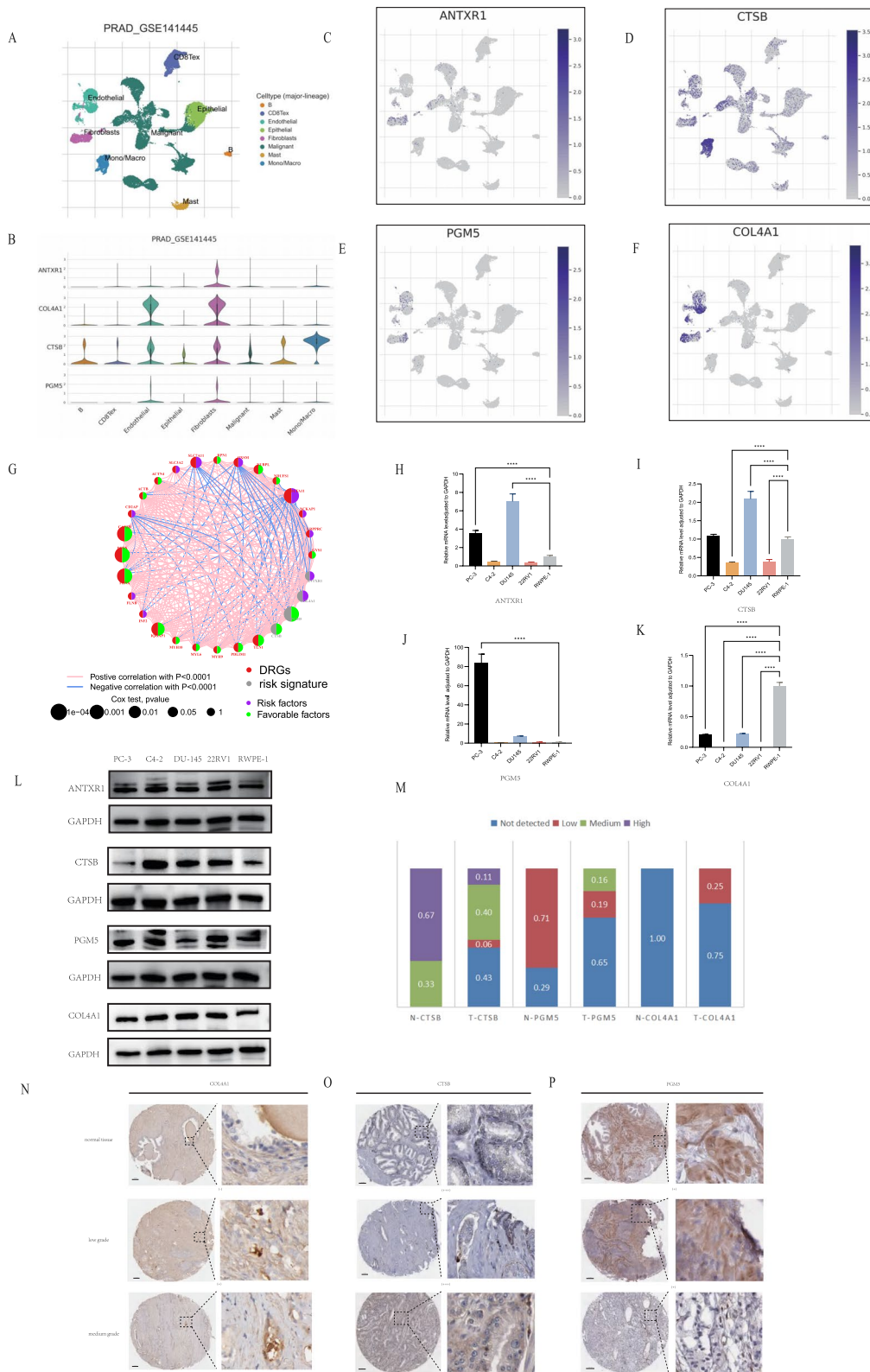


**Fig. 5** (See legend on previous page.)

predictions difficult. However, the risk scores for gene-cluster-I and gene-cluster-III have clear boundaries, corresponding to high risk and low risk, respectively. In simple terms, the presence of gene-cluster-II removes the confounding factors within the DRG cluster and provides a clearer prediction of prognosis. The high-risk group exhibits gene mutations in DRGs such as MYH10, FLNB, and TLN1, which may hinder the normal progression of disulfidptosis and correspond to the population represented by cluster A with low levels of disulfidptosis.

In this study, the TME in the low-risk group was populated with plasma cells, NK cells, resting mast cells, and M0 macrophages. Based on the prediction results of The Cancer Immunome Atlas (TICA), irrespective of the expression levels of immune checkpoints, ICB therapy performed better in the low-risk group (Supplementary Materials 1). The high-risk group was infiltrated by Treg cells and M2 macrophages, and both the tumor matrix score and the tumor mutational burden were elevated, confirming the inhibitory TME caused by repressed disulfidptosis. Currently, potential biomarkers that may affect the efficacy of prostate cancer immune checkpoint inhibitors include TMB, MSI/MMR (Microsatellite instability/Mismatch repair), CDK12, PD-L1 gene, among others [20]. The NCCN guidelines also recommend pembrolizumab monotherapy for mCRPC patients with  $TMB \geq 10\text{mt/Mb}$  or dMMR/MSI-H [21]. However, in different immune combination therapies, there are discrepancies in the predictive role of biomarkers. For instance, in the results of CheckMate 9KD [22], no clear association was found between homologous recombination deficiency (HRD) or TMB and the response to nivolumab monotherapy combined with docetaxel. The COSMIC-021 trial [23] used cabozantinib combined with atezolizumab to treat CRPC, but no correlation was observed between PD-L1 status and therapeutic effect. In the high-risk group of this study, TMB was high, prognosis was poor, and PD-L1 expression levels were low. Whether promotion of disulfidptosis could change these indicators and alter the efficacy of ICB, warranting further attention.

Among the four risk signature genes, not all genes show differential expression between tumor specimens and normal tissues. Interestingly, at the protein level, all molecules were expressed in tumor cells, with no negative results. This does not affect the predictive accuracy of the risk model as a whole, a fact confirmed by its predictive ability in the external testing set. Specifically, ANTXR1 is a prognostic molecule that increases the risk score. It can connect the cytoskeleton to ECM molecules, regulating cell adhesion, cell migration, or ECM homeostasis [24]. Past research has shown that it can inhibit breast cancer and glioma cell migration [25,

26]. Yet in PCa, it is mainly expressed in cancer-associated fibroblasts (CAFs), and qPCR also revealed its high expression in late-stage CRPC cells. At the protein activity level, its relative expression in tumor tissue was higher. COL4A1 shows low intensity expression in cancer tissues. Previous studies have shown that COL4A1 is concentrated in the CAFs and endothelial cells of gliomas, pancreatic cancer, melanoma, and gastric cancer. It is positively correlated with TME inhibitory factors such as Treg, M2, and TAM, and is associated with poor cancer prognosis [27]. However, in PCa, Thomas Van den Broeck et al. [28] believe that COL4A1 is a factor inhibiting cancer cell migration. Based on WB and HPA results, our model in this study leans more towards its pro-cancer role. PGM5 encodes a phosphoglucomutase involved in the process of glucose metabolism. Jian Sun et al. [29] believe it can inhibit the proliferation and migration of PCa cells. In this study, PGM5 showed low expression in DU145 and PC-3, while its expression level was high in 22RV1. In the HPA results, PGM5 levels were also higher in normal tissues and low-grade tumors, suggesting that PGM5 as an inhibitor of tumor cell invasion and metastasis deserves further in-depth study. CTSB encodes a cysteine protease involved in protein degradation under normal physiological conditions and extracellular matrix remodeling [30]. It can degrade components of the extracellular matrix, promoting tumor cell invasion into surrounding tissues and blood vessels. In tumor cells, CTSB can also damage mitochondrial membranes promoting ferroptosis [31]. In the WB results of this study, CTSB level was low in RWPE-1, but was expressed in various stages of tumor cell lines, consistent with its characteristics promoting metastasis.

In disulfidptosis, both the accumulation of disulfidptosis and the disruption of the actin cytoskeleton are not closely related to androgens, but they have the potential to shape the TME. These features may circumvent the resistance of CRPC, making DRG-related treatment targets worth continuous attention. Our study has some limitations. First, the prognostic model based on public relations database needs further clinical verification for its accuracy. Secondly, the signature proteins and pathways in PCa disulfidptosis have not been studied in depth. Finally, the connection between immunology and disulfidptosis is mostly based on bioinformatics analysis, lacking direct evidence.

## Conclusion

In this study, based on DRG, we stratified PCa patients into two clusters (A and B) and established a risk score model based on their differential genes. This model can be used to judge the prognosis and immune-related

functions of PCa. The cluster B population exhibited higher levels of disulfidptosis gene expression, lower risk, better prognosis, high immune cell infiltration, and greater sensitivity to immune checkpoint blockade (ICB). Conversely, cluster A showed the opposite characteristics. This suggests that DRGs serve as stratifying features and potential therapeutic targets in PCa. Simultaneously, we connected DRGs with clinical pathological characteristics to construct a nomogram, providing clinicians with a quantitative method to assess the prognosis of PCa patients.

## Supplementary Information

The online version contains supplementary material available at <https://doi.org/10.1186/s13062-024-00544-4>.

Figure S1. (A, B) qPCR and WB were used to verify the CRISPR-Cas9 knock-out efficiency of SLC7A11 in DU145 cells. (C, D) qPCR and WB were used to verify the CRISPR-Cas9 knock-out efficiency of SLC7A11 in PC-3 cells. (E, F) A scratch assay demonstrated that SLC7A11 knockout (SLC7A11-KO) inhibited the migration of DU145 and PC-3 cells. (G, H) Transwell assays confirmed that SLC7A11-KO inhibited the invasion of DU145 and PC-3 cells. (I) Flow cytometry analysis showed that DU145 cells exhibited minimal late-stage apoptosis after 16 hours of culture in a glucose-free medium, whereas SLC7A11 overexpression (SLC7A11-OE) significantly induced late-stage apoptosis. This apoptotic effect was reversed in SLC7A11-KO cells. (J) Flow cytometry analysis revealed significant late-stage apoptosis in PC-3 cells after 16 hours of glucose-free culture. SLC7A11-OE further enhanced late-stage apoptosis, while this effect was reversed in SLC7A11-KO cells.

Additional file 1.

Figure S2: Immunohistochemical staining of SLC7A11 in prostate cancer and normal prostate tissues. (A) Representative images of SLC7A11 expression in normal prostate tissues. (B) Representative images of SLC7A11 expression in prostate cancer tissues. The staining intensity was assessed using a semi-quantitative scoring system, where "-" indicates no expression, "+" indicates low expression, "++" indicates moderate expression, and "+++" indicates high expression. In prostate cancer tissues, SLC7A11 expression was significantly higher compared to normal tissues, suggesting a potential role in tumor progression.

Additional file 2.

Additional file 3.

Additional file 4.

Additional file 5.

Additional file 6. Supplementary Materials 1

Additional file 7. Supplementary Materials 2

Additional file 8.

## Acknowledgements

Immunohistochemical images in this study were obtained from the Human Protein Atlas (HPA). All the data of HPA in the knowledge resource is open access to allow scientists both in academia and industry to freely access the data for exploration of the human proteome. Special thanks are given to the HPA for data disclosure.

## Author contributions

ZK, NX, YW design the study; ZK, ZHW and R-CG wrote the manuscript; D-NC, R-CG collected relevant data and information; ZKD-NC, Q-SZ and X-YX analyzed data. All authors approved the submitted version. YW is the correspondence author. NX is co-correspondence author.

## Funding

This study was supported by Major Research Project for Young and Middle-aged Scientists of the Fujian Provincial Health Commission (Grant number: 2022ZQNZD006), and Science and Technology Innovation Joint fund of Fujian Province (Grant number: 2023Y9078).

## Availability of data and materials

The datasets presented in this study can be found in online repositories. The names of the repository/repositories and accession number(s) can be found in the article/Supplementary Material.

## Declarations

### Ethics approval and consent to participate

The studies involving human participants were reviewed and approved by the Institutional Ethics Committee of First Affiliated Hospital of Fujian Medical University.

### Competing interests

The authors declare no competing interests.

### Author details

<sup>1</sup>Department of Urology, Urology Research Institute, the First Affiliated Hospital, Fujian Medical University, Fuzhou 350212, China. <sup>2</sup>Department of Urology, National Regional Medical Centre, Binhai Campus of the First Affiliated Hospital, Fujian Medical University, Fuzhou 350212, China. <sup>3</sup>Fujian Key Laboratory of Precision Medicine for Cancer, the First Affiliated Hospital, Fujian Medical University, Fuzhou 350212, China.

Received: 10 July 2024 Accepted: 7 October 2024

Published online: 23 October 2024

## References

- Sandhu S, Moore CM, Chiong E, Beltran H, Bristow RG, Williams SG. Prostate cancer. *Lancet*. 2021;398(10305):1075–90.
- Wang S, Wei W, Ma N, Qu Y, Liu Q. Molecular mechanisms of ferroptosis and its role in prostate cancer therapy. *Crit Rev Oncol Hematol*. 2022;176:103732.
- Kadeerhan, G, Xue, B, Wu, XL, et al. Incidence trends and survival of metastatic prostate cancer with bone and visceral involvement: 2010–2019 surveillance, epidemiology, and end results. *Front Oncol*. 2023;13:1201753.
- Goji T, Takahara K, Negishi M, Katoh H. Cystine uptake through the cystine/glutamate antiporter xCT triggers glioblastoma cell death under glucose deprivation. *J Biol Chem*. 2017;292(48):19721–32.
- Liu X, Nie L, Zhang Y, Yan Y, Wang C, Colic M, Olszewski K, Horbath A, Chen X, Lei G, Mao C, Wu S, Zhuang L, Poyurovsky MV, James You M, Hart T, Billadeau DD, Chen J, Gan B. Actin cytoskeleton vulnerability to disulfidptosis stress mediates disulfidptosis. *Nat Cell Biol*. 2023;25(3):404–14.
- Pompe RS, Gild P, Karakiewicz PI, Bock LP, Schlomm T, Steuber T, Graefen M, Huland H, Tian Z, Tilki D. Long-term cancer control outcomes in patients with biochemical recurrence and the impact of time from radical prostatectomy to biochemical recurrence. *Prostate*. 2018;78(9):676–81.
- Van den Broeck T, van den Bergh RCN, Arfi N, Gross T, Moris L, Briers E, Cumberbatch M, De Santis M, Tilki D, Fanti S, Fossati N, Gillissen S, Grummet JP, Henry AM, Laldas M, Liew M, Rouvière O, Pecanka J, Mason MD, Schoots IG, van Der Kwast TH, van Der Poel HG, Wiegel T, Willemsse PM, Yuan Y, Lam TB, Cornford P, Mottet N. Prognostic value of biochemical recurrence following treatment with curative intent for prostate cancer: a systematic review. *Eur Urol*. 2019;75(6):967–87.
- Mayakonda A, Lin DC, Assenov Y, Plass C, Koeffler HP. Maftools: efficient and comprehensive analysis of somatic variants in cancer. *Genome Res*. 2018;28(11):1747–56.
- Ritchie ME, Phipson B, Wu D, Hu Y, Law CW, Shi W, Smyth GK. Limma powers differential expression analyses for RNA-sequencing and microarray studies. *Nucl Acids Res*. 2015;43(7):e47.

10. Wilkerson MD, Hayes DN. ConsensusClusterPlus: a class discovery tool with confidence assessments and item tracking. *Bioinformatics*. 2010;26(12):1572–3.
11. Hänzelmann S, Castelo R, Guinney J. GSVA: gene set variation analysis for microarray and RNA-seq data. *BMC Bioinf*. 2013;16(14):7.
12. Brunson JC. ggalluvial: layered grammar for alluvial plots. *J Open Source Softw*. 2020;5(49):2017.
13. Chen S, Zhu G, Yang Y, Wang F, et al. Single-cell analysis reveals transcriptomic remodellings in distinct cell types that contribute to human prostate cancer progression. *Nat Cell Biol*. 2021;23(1):87–98.
14. Ritch C, Cookson M. Recent trends in the management of advanced prostate cancer. *F1000Res*. 2018;7:F1000 Faculty Rev-1513.
15. Cha HR, Lee JH, Ponnazhagan S. Revisiting immunotherapy: a focus on prostate cancer. *Cancer Res*. 2020;80(8):1615–23.
16. Madan RA, Gully JL. Finding an immunologic beachhead in the prostate cancer microenvironment. *J Natl Cancer Inst*. 2019;111(3):219–20.
17. Tang R, Xu J, Zhang B, Liu J, Liang C, Hua J, Meng Q, Yu X, Shi S. Ferroptosis, necroptosis, and pyroptosis in anticancer immunity. *J Hematol Oncol*. 2020;13(1):110.
18. Yatim N, Jusforgues-Saklani H, Orozco S, Barreira da Silva SOR, Reis e Sousa C, Green DR, Oberst A, Albert ML. RIPK1 and NF- $\kappa$ B signaling in dying cells determines cross-priming of CD8 T cells. *Science*. 2015;350:328–34.
19. The ST, Cytoskeleton A, Motility A-B. The actin cytoskeleton and actin-based motility. *Cold Spring Harb Perspect Biol*. 2018;10(1): a018267.
20. Rebuzzi SE, Rescigno P, Catalano F, Mollica V, Vogl UM, Marandino L, Mas-sari F, Pereira Mestre R, Zanardi E, Signori A, Buti S, Bauckneht M, Gillesen S, Banna GL, Fornarini G. Immune checkpoint inhibitors in advanced prostate cancer: current data and future perspectives. *Cancers (Basel)*. 2022;14(5):1245.
21. Moses KA, Sprenkle PC, Bahler C, Box G, Carlsson SV, Catalona WJ, Dahl DM, Dall'Era M, Davis JW, Drake BF, Epstein JI, Etzioni RB, Farrington TA, Garraway IP, Jarrard D, Kauffman E, Kaye D, Kibel AS, LaGrange CA, Maroni P, Ponsky L, Reys B, Salami SS, Sanchez A, Seibert TM, Shaneyfelt TM, Smaldone MC, Sonn G, Tyson MD, Vapiwala N, Wake R, Washington S, Yu A, Yuh B, Berardi RA, Freedman-Cass DA. NCCN Guidelines<sup>®</sup> Insights: Prostate Cancer Early Detection, Version 1.2023. *J Natl Compr Canc Netw*. 2023;21(3):236–246.
22. Fizazi K, Retz M, Petrylak DP, Goh JC, Perez-Gracia J, Lacombe L, Zschäbitz S, Burotto M, Mahammedi H, Gravis G, Bastos DA, McCune SL, Vázquez Limón JC, Kwan EM, Castellano D, Fléchon A, Saad F, Grimm MO, Shaffer DR, Armstrong AJ, Bhagavatheswaran P, Amin NP, Ünsal-Kaçmaz K, Wang X, Li J, Loehr A, Pachynski RK. Nivolumab plus rucaparib for metastatic castration-resistant prostate cancer: results from the phase 2 CheckMate 9KD trial. *J Immunother Cancer*. 2022;10(8): e004761.
23. Agarwal N, McGregor B, Maughan BL, Dorff TB, Kelly W, Fang B, McKay RR, Singh P, Pagliaro L, Dreicer R, Srinivas S, Loriot Y, Vaishampayan U, Goel S, Curran D, Panneerselvam A, Schwickart M, Choueiri TK, Pal S. Cabozantinib in combination with atezolizumab in patients with metastatic castration-resistant prostate cancer: results from an expansion cohort of a multicentre, open-label, phase 1b trial (COSMIC-021). *Lancet Oncol*. 2022;23(7):899–909.
24. Feng F, Cheng B, Cheng B, Jia Y, Zhang M, Xu F. ANTXR1 as a potential sensor of extracellular mechanical cues. *Acta Biomater*. 2023;1(158):80–6.
25. Chen D, Bhat-Nakshatri P, Goswami C, Badve S, Nakshatri H. ANTXR1, a stem cell-enriched functional biomarker, connects collagen signaling to cancer stem-like cells and metastasis in breast cancer. *Cancer Res*. 2013;73(18):5821–33.
26. Dong Z, Zhang J, Niu L, Hou G, Gao Z, Yang Q. miR-381-3p involves in glioma progression by suppressing tumor-promoter factor ANTXR1. *Comput Math Methods Med*. 2021;16(2021):4883509.
27. Shin HJ, Gil M, Lee IS. Association of elevated expression levels of COL4A1 in stromal cells with an immunosuppressive tumor microenvironment in low-grade glioma, pancreatic adenocarcinoma, skin cutaneous melanoma, and stomach adenocarcinoma. *J Pers Med*. 2022;12(4):534.
28. Van den Broeck T, Moris L, Gevaert T, Davicioni E, Boeckx B, Lambrechts D, Helsen C, Handle F, Ghesquière B, Soenen S, Smeets E, Eerlings R, El Kharraz S, Devlies W, Karnes RJ, Lotan T, Van Poppel H, Joniau S, Claessens F. Antizyme inhibitor 1 regulates matrikine expression and enhances the metastatic potential of aggressive primary prostate cancer. *Mol Cancer Res*. 2022;20(4):527–41.
29. Sun J, Wang F, Zhou H, Zhao C, Li K, Fan C, Wang J. Downregulation of PGM5 expression correlates with tumor progression and poor prognosis in human prostate cancer. *Discov Oncol*. 2022;13(1):63.
30. Wyczalkowska-Tomasik A, Paczek L. Cathepsin B and L activity in the serum during the human aging process: cathepsin B and L in aging. *Arch Gerontol Geriatr*. 2012;55:735–8.
31. Nagakannan P, Islam MI, Conrad M, Eftekharpour E. Cathepsin B is an executioner of ferroptosis. *Biochim Biophys Acta Mol Cell Res*. 2021;1868(3): 118928.

## Publisher's Note

Springer Nature remains neutral with regard to jurisdictional claims in published maps and institutional affiliations.